eNeuro

Research Article: New Research
Disorders of the Nervous System

Temporal Alterations in White Matter in An *App* Knock-In Mouse Model of Alzheimer's Disease

Zachery D. Morrissey,[1,2,3] Jin Gao,[4,5] Aashutosh Shetti,[3] Wenping Li,[6] Liang Zhan,[7] Weiguo Li,[8,5,9] Igor Fortel,[8] Takaomi Saido,[10] Takashi Saito,[11] Olusola Ajilore,[2] Stephanie M. Cologna,[6] Orly Lazarov,[3] and Alex D. Leow[2,8,12]

[1]Graduate Program in Neuroscience, University of Illinois Chicago, Chicago, Illinois 60612, [2]Department of Psychiatry, University of Illinois Chicago, Chicago, Illinois 60612, [3]Department of Anatomy & Cell Biology, University of Illinois Chicago, Chicago, Illinois 60612, [4]Department of Electrical & Computer Engineering, University of Illinois Chicago, Chicago, Illinois 60607, [5]Preclinical Imaging Core, University of Illinois Chicago, Chicago, Illinois 60612, [6]Department of Chemistry, University of Illinois Chicago, Chicago, Illinois 60607, [7]Department of Electrical & Computer Engineering, University of Pittsburgh, Pittsburgh, Pennsylvania 15261, [8]Department of Bioengineering, University of Illinois Chicago, Chicago, Illinois 60607, [9]Department of Radiology, Northwestern University, Chicago, Illinois 60611, [10]Laboratory for Proteolytic Neuroscience, RIKEN Center for Brain Science, Wako 351-0198, Japan, [11]Department of Neurocognitive Science, Institute of Brain Science, Nagoya City University, Nagoya 467-8601, Japan, and [12]Department of Computer Science, University of Illinois Chicago, Chicago, Illinois 60607

Received Nov. 27, 2023; revised Jan. 5, 2024; accepted Jan. 17, 2024.

The authors declare no competing financial interests.

Z.D.M., J.G., A.S., W.L., L.Z., W.L., O.A., S.M.C., O.L., and A.D.L. designed research; Z.D.M., J.G., A.S., W.L., and W.L. performed research; Z.S.M., A.S., W.L., L.Z., and I.F. analyzed data; Takaomi Saido, Takashi Saito, and S.M.C. contributed unpublished reagents/analytic tools, Z.D.M., J.G., A.S., W.L., O.A., S.M.C., O.L., and A.D.L. wrote the paper.

We would like to thank Dr. Alexander Demos for assistance with statistical modeling.

This study was supported by 10.13039/100000049NIH AG056782, AG071243, MH125928 (A.D.L., L.Z.), AG07694, AG033570, AG062251, AG060238 (O.L.), T32MH067631, T32AG057468 (Z.D.M.), R01NS114413, R01NS124784 (S.M.C.), 10.13039/100000001 National Science Foundation (NSF) Information and Intelligent Systems (IIS) 2045848 (L.Z.), NSF CAREER 2143920 (S.M.C.), and Together Strong Niemann-Pick Disease, Type C (NPC) Foundation (W.L., S.M.C.).

Correspondence should be addressed to Orly Lazarov at olazarov@uic.edu.

Abstract

Alzheimer's disease (AD) is the most common form of dementia and results in neurodegeneration and cognitive impairment. White matter (WM) is affected in AD and has implications for neural circuitry and cognitive function. The trajectory of these changes across age, however, is still not well understood, especially at earlier stages in life. To address this, we used the *App*$^{NL\text{-}G\text{-}F/NL\text{-}G\text{-}F}$ knock-in (APPKI) mouse model that harbors a single copy knock-in of the human amyloid precursor protein (*APP*) gene with three familial AD mutations. We performed *in vivo* diffusion tensor imaging (DTI) to study how the structural properties of the brain change across age in the context of AD. In late age APPKI mice, we observed reduced fractional anisotropy (FA), a proxy of WM integrity, in multiple brain regions, including the hippocampus, anterior commissure (AC), neocortex, and hypothalamus. At the cellular level, we observed greater numbers of oligodendrocytes in middle age (prior to observations in DTI) in both the AC, a major interhemispheric WM tract, and the hippocampus, which is involved in memory and heavily affected in AD, prior to observations in DTI. Proteomics analysis of the hippocampus also revealed altered expression of oligodendrocyte-related proteins with age and in APPKI mice. Together, these results help to improve our understanding of the development of AD pathology with age, and imply that middle age may be an important temporal window for potential therapeutic intervention.

Key words: white matter; *App*$^{NL\text{-}G\text{-}F/NL\text{-}G\text{-}F}$; oligodendrocytes; myelin; Alzheimer's disease; DTI

Significance Statement

Alzheimer's disease (AD) is a progressive neurodegenerative disorder that develops decades before onset of cognitive impairment. The trajectory of the pathology across age in white matter (WM), however, is still not well understood. Here, we used an *App*$^{NL\text{-}G\text{-}F/NL\text{-}G\text{-}F}$ knock-in mouse model to study WM using diffusion tensor imaging (DTI) and biochemical analyses. We observed reduced fractional anisotropy, a WM integrity proxy, in the hippocampus and anterior commissure between middle and late age. Notably, we observed changes in oligodendrocytes in middle age that preceded the changes in DTI. Together, this suggests that alterations in oligodendrocyte homeostasis may contribute to changes in WM in middle age. These results may serve as an important biomarker, therapeutic target, and provide new insight into the progression of AD.

Introduction

Alzheimer's disease (AD) is the most common form of dementia. The early mechanisms underlying the pathology of AD, however, are still not well understood. One of the major challenges is that alterations in the brain take place many years before a clear behavioral manifestation can be diagnosed. Thus, observations in mouse models of AD may provide important information on these early processes. White matter (WM)-related alterations have been implicated in AD (Bartzokis, 2011). One of the earliest descriptions of WM changes in AD was in *postmortem* histological experiments by Brun & Englund in the 1980s, where they observed topographical and symmetrical loss of myelinated axons and WM lesions in AD patients (Brun and Englund, 1986). The development of magnetic resonance imaging (MRI), and in particular diffusion tensor imaging (DTI) (Basser et al., 1994), has allowed for the non-invasive study of brain structure in detail. Before the onset of cognitive impairment, brain atrophy—particularly in the hippocampus—is arguably one of the most reliable markers for AD (Fox et al., 1996; Ridha et al., 2006; Webster et al., 2014). DTI studies have also provided evidence that, in addition to changes in gray matter (GM) (Weston et al., 2015), WM is also degenerated in AD (Bozzali, 2002; Lo Buono et al., 2020). Furthermore, evidence suggests that alterations in WM appear early in the course of the disease, even before the well-characterized atrophy and neurodegeneration in GM (Fischer et al., 2015; Nasrabady et al., 2018). Thus, understanding the trajectory of WM changes may help us to better understand the development of AD and identify potential biomarkers for therapeutic intervention.

During development, there are orchestrated waves of oligodendrogenesis and myelination (El Waly et al., 2014). Originally thought to be static after development, oligodendrogenesis and myelination continue throughout adulthood (Blakemore, 1972; Kaplan and Hinds, 1980; Menn et al., 2006; El Waly et al., 2014), and is homeostatically regulated (Hughes et al., 2013; Hill et al., 2018). Recently, it has been found that adult oligodendrogenesis and myelination are actively involved in learning and memory (McKenzie et al., 2014; Steadman et al., 2020; Chen et al., 2021); thus, experience-dependent oligodendrocyte and myelin plasticity are likely important for healthy cognitive function (Williamson and Lyons, 2018; Xin and Chan, 2020; McNamara and Miron, 2021). Therefore, disruptions in WM and oligodendrocyte homeostasis could have an important role in cognitive decline in AD.

A small percentage of AD patients have mutations in the amyloid precursor protein (*APP*) and presenilin-1 (*PSEN1*) and presenilin-2 (*PSEN2*) genes that result in an autosomal dominant form of the disease, known as familial AD (FAD). Despite the low prevalence of FAD, study of the genetics of these FAD patients has led to the development of many commonly used AD mouse models (Webster et al., 2014). Here, we used the $App^{NL\text{-}G\text{-}F/NL\text{-}G\text{-}F}$ knock-in (APPKI) mouse model of AD developed by Saito et al. (2014) that contains a single copy knock-in of human *APP* with the Swedish (K670N, M671L), Arctic (E693G), and Beyreuther/Iberian (I716F) FAD mutations. We performed *in vivo* DTI of APPKI mice in early (4 months), middle (10 months), and late (>15 months) age groups to measure the macroscale structural properties of the brain across age from just before the onset of Aβ plaque deposition and cognitive impairment. We observed that APPKI mice had reduced fractional anisotropy (FA) in multiple regions between middle and late age, suggesting that this time window is when potential microstructural impairment occurs. In 10-month-old mice, we observed that APPKI mice had a greater number of oligodendrocytes in the hippocampus and anterior commissure (AC). Despite this, we observed a reduction in lipid staining in the AC, suggesting that more oligodendrocytes did not correspond to more myelin. Furthermore, proteomics analysis of the hippocampus showed multiple oligodendrocyte-related proteins with altered expression by age and in APPKI. Our results suggest that there are WM-related alterations in APPKI mice across age, and that changes in the oligodendrocyte population precede observed changes in DTI. Together, these results offer further evidence for the contribution of myelin and oligodendrocyte dynamics to the pathological development of AD.

Materials and Methods

Animals. Animal protocols were approved by the University of Illinois Chicago Institutional Animal Care and Use Committee. Mice used in this study were from a C57Bl/6 background. APPKI mice were generated by Saito et al. (2014). Tail samples were obtained from mice at time of weaning to test for APPKI genotype. Animals were housed in standard housing conditions with up to five mice per cage on a 12 h light–dark cycle and allowed to feed and drink *ad libitum*. Details for mice scanned in this study are shown in Extended Data Table 1-1.

In vivo *MRI acquisition.* Animals were anesthetized using 1–2% isoflurane and imaged using a 9.4 T Agilent MRI system (Santa Clara, California, USA) as described previously (Morrissey et al., 2023). Briefly, mice were secured using a bite bar to restrict head motion, and ambient temperature and respiratory rate were monitored continuously during the scan using an SAII gating and monitoring system for small animals (SA Instruments, New York, USA). A T_2 – weighted fast-spin echo sequence was acquired using the following parameters: TR = 2,000 ms, TE = 10 ms, echo train length = 8, slice thickness =1 mm, number of slices = 20, FOV = 19.2 mm × 19.2 mm, matrix size =128 × 128, acquisition time = 2 min 12 s.

A 3D shimming was performed prior to diffusion-weighted imaging (DWI) to mitigate magnetic field inhomogeneity, with both first- and second-order shims optimized in a user-defined shim voxel (20 mm × 20 mm × 20 mm) covering the brain volume for DWI (Vanzijl et al., 1994). DWI images were obtained using a 12-direction gradient table and b_0 images (TR = 1,800 ms, TE = 23.22 ms, slice thickness =1 mm, number of slices =10, number of averages = 32, b = 1,000 s/mm^2, FOV = 19.2 mm × 19.2 mm, matrix size =128 × 128, acquisition time =1 h 42 min 35 s).

DTI analysis. T_2 – weighted and DWI images were converted from raw digital imaging and communications in medicine format to Neuroimaging Informatics Technology Initiative (NIfTI) format using dcm2niix (Li, 2016). A brain mask was then created for both T_2 – weighted and DWI images by manually outlining the brain using fsleyes (version 0.26.4) from the FMRIB Software Library (FSL) 6.0 (Smith et al., 2004). The diffusion tensor model was applied using the dtifit program from FSL (Jenkinson et al., 2012). The Waxholm space atlas (Johnson et al., 2010) was used to register atlas labels to each subject space by doing a two-step registration using the FSL flirt linear registration tool with 12 degrees of freedom (Fig. 1*b*). First, the high resolution T_2 – weighted atlas image was registered to each subject's T_2 – weighted image. Next, the subject's T_2 – weighted image was registered to their respective b_0 DWI image. Finally, the transformation matrices from these two steps were concatenated to transform the atlas labels to the subject's b_0 image using nearest neighbor interpolation. The FA output from dtifit was used with the registered atlas labels to measure the mean FA values for each region for each subject.

Immunohistochemistry. Mice were anesthetized with isoflurane and transcardially perfused with ice-cold phosphate-buffered saline (PBS) followed by 4% w/v paraformaldehyde (PFA) to fix the brain. The brain was then extracted and placed in 4% w/v PFA to fix overnight at 4°C. The following day, brains were transferred to 30% w/v sucrose in PBS at 4°C for at least 3 d until the brain was fully submerged. Brains were frozen and coronal sections were cut at 50 µm thickness using a Leica SM2010R microtome. Free-floating sections were stored in 96-well plates containing a cryoprotectant composed of 30% v/v ethylene glycol and 30% v/v glycerol in PBS at −20°C.

Free-floating sections were washed three times for 5 min with PBS and mounted onto glass slides. Heat-mediated antigen retrieval was performed using 10 mM sodium citrate (pH 6) with 0.05% v/v Tween-20 at 95°C for 10 min. Slides were cooled to room temperature for 20 min and washed with PBS. Permeabilization and blocking were performed by adding PBS with 0.3 M glycine, 0.25% v/v Triton X-100, 5% v/v normal donkey serum, and 2% w/v bovine serum albumin for 1 h. Primary antibodies were then added in blocking buffer solutions at the specified dilutions and incubated for 3 d at 4°C. Primary antibodies used: 1:100 rabbit anti-OLIG2 (abcam ab109186) and 1:200 goat anti-platelet-derived growth factor receptor α (PDGFRA; R&D Systems AF1062). The sections were washed three times for 5 min with PBS. The secondary antibodies were added to blocking buffer at the specified dilutions and incubated for 1 h at room temperature under darkness. Secondary antibodies: 1:500 donkey anti-rabbit Cy3 (Jackson Immuno 711–165–152) and 1:500 donkey anti-goat Alexa Fluor 488 (Jackson Immuno 705–545–147). Sections were washed three times for 5 min with PBS; during the second wash, 5 µg/mL DAPI was added to stain nuclei. Sections were washed with 70% ethanol for 5 min and autofluorescence eliminator reagent (Millipore 2160) was added drop-wise to each section. Sections were then washed with 70% ethanol twice for 2 min. After the last wash, sections were allowed to dry and glass coverslips were mounted with polyvinyl alcohol DABCO (PVA-DABCO) antifade. The coverslips were sealed with clear nail polish, and slides were stored in a slide box at 4°C until imaged.

For Fluoromyelin Red staining, free-floating 50 µm coronal sections were washed three times for 5 min with PBS. Sections were permeabilized with PBS containing 0.3 M glycine and 0.1% v/v Triton X-100 for 20 min. Sections were incubated with 1:300 Fluoromyelin Red (ThermoFisher F34652) for 3 h. Sections were washed three times with PBS for 10 min. During the second wash, 5 µg/mL DAPI was added to stain nuclei. Sections were mounted onto slides and glass coverslips were mounted using PVA-DABCO and sealed as described above.

Stereological quantification. Wild-type and APPKI serial 50 µm coronal sections were selected for stereological quantification of oligodendrocytes and oligodendrocyte precursor cells (OPCs) using the markers OLIG2 and PDGFRA using a Zeiss Axio Imager microscope system. The experimenter was blinded to the animal genotype during counting. The optical fractionator workflow from Stereo Investigator version 2020.2.3 (MicroBrightfield, Inc.) was used for quantification (Stereo Investigator, 2020). The ROIs were demarcated at 5 × magnification and quantified at 63 × magnification. The estimated number of cells for each marker was normalized to the ROI volume for each subject.

The parameters used for the optical fractionator protocol in Stereo Investigator are shown for the AC in Extended Data Table 2-1 and for the hippocampus in Extended Data Table 3-1. For each animal, the estimated number of cells N for each marker is defined as

$$N = \sum_{i=1}^{n} Q_i^- \cdot \frac{\bar{t}}{h} \cdot \frac{1}{asf} \cdot \frac{1}{ssf} \tag{1}$$

for n sections, where Q_i^- is the raw number of cells counted for the ith section, $\bar{t}$ is the mean section thickness, h is the optical disector height, asf is the area sampling fraction, and ssf is the section sampling fraction (Gundersen and Jensen, 1987; Gundersen et al., 1999; Keuker et al., 2001; Stereo Investigator, 2020). The estimated number of cells was normalized to the estimated volume of each region for each animal. Gundersen's coefficient of error (CE) is defined as

$$\mathrm{CE} = \frac{\sqrt{\mathrm{Var}_{\mathrm{total}}}}{s^2}, \tag{2}$$

where $s^2 = \sum_{i=1}^{n} Q_i^-$ is the variance due to noise for n sections, and $\mathrm{Var}_{\mathrm{total}} = s^2 + \mathrm{Var}_{\mathrm{SRS}}$ is the total variance, where $\mathrm{Var}_{\mathrm{SRS}}$ is the systematic random sampling variance, defined as

$$\mathrm{Var}_{\mathrm{SRS}} = \frac{3\left(\left(\sum_{i=1}^{n}\left(Q_i^-\right)^2\right) - s^2\right) - 4\sum_{i}^{n-1} Q_i^- Q_{i+1}^- + \sum_{i=1}^{n-2} Q_i^- Q_{i+2}^-}{240}. \quad (3)$$

Western blot analysis. Mice were anesthetized with isoflurane and transcardially perfused with ice-cold PBS. The brain was extracted and placed into a Petri dish on ice containing ice-cold PBS. The hippocampus was dissected and snap-frozen in microcentrifuge tubes in liquid nitrogen and stored at −80°C until processed. Hippocampus tissue was thawed on ice, homogenized, and lysed in radioimmunoprecipitation assay buffer with protease and phosphatase inhibitors (Sigma P8340–5ML, Thermo 78420). Cells were lysed by sonicating three times for 15 s at 30% amplitude. Lysates were centrifuged at 16,000*g* for 15 min at 4°C and the supernatant was transferred to sterile microcentrifuge tubes. Protein estimation of lysate samples was performed using a bicinchoninic acid (BCA) assay (Thermo 23223 and 23224). Samples were prepared for sodium dodecyl sulphate (SDS)-PAGE at 1 µg/µL concentration with 10 × reducing agent (Invitrogen B0009) and 4 × sample buffer (Invitrogen B0007).

Samples were boiled at 95°C for 5 min prior to SDS-PAGE. SDS-PAGE was performed using 4–12% Bis–Tris polyacrylamide gels (Invitrogen NW04122BOX) at 200 V for 22 min. An iBlot2 dry blotting system (Thermo IB21001) was used to transfer samples from the polyacrylamide gel to a nitrocellulose membrane (20 V for 1 min, 23 V for 4 min, and 25 V for 2 min). Membranes were blocked with 5% w/v non-fat dairy milk powder in Tris-buffered saline with 0.1% v/v Tween-20 (TBST) for 1 h and incubated with primary antibodies at the specified dilutions in blocking buffer overnight at 4°C. Primary antibodies: 1:1,000 rabbit anti-OLIG2 (abcam ab109186) and 1:5,000 mouse anti-actin (Invitrogen MA5-11869). Membranes were washed three times for 15 min with TBST and incubated with horseradish peroxidase (HRP)-conjugated secondary antibodies at the specified dilutions for 1 h at room temperature. Secondary antibodies used: 1:10,000 anti-mouse IgG HRP (Promega W402B) and 1:10,000 anti-rabbit IgG HRP (Promega W4018). Membranes were then washed three times for 15 min with TBST. SuperSignal West PICO Plus chemiluminescent substrate (Thermo 1863094 and 1863095) was applied to the membranes and the membranes were exposed onto autoradiography films in a dark room.

Autoradiography films were scanned to a computer and the images were analyzed using FIJI (Schindelin et al., 2012). Images were converted to grayscale and the Analyze > Gels tool was used to estimate the gray value density for each band. The gray value density for the protein of interest was then calculated relative to the actin loading control for each sample. The relative values were then normalized to the mean of the wild-type group for comparing across groups.

Microscopy. Confocal images were acquired using a Zeiss LSM 710 confocal microscope. Maximum intensity *z*-projections were used for representative images. Postprocessing of representative images was performed using the brightness/contrast, remove outliers, and subtract background tools in FIJI (Schindelin et al., 2012). The 4 × tile-stitched images of Fluoromyelin Red staining were acquired using a Keyence BZ-X800 microscope. For Fluoromyelin Red fluorescence intensity analysis, *z*-stack images of midline AC were acquired using the same imaging parameters, and sum intensity *z*-projections were used for quantification.

Mouse hippocampal lysis and protein digestion for proteomics. Three male wild-type C57Bl/6 and three male $App^{NL\text{-}G\text{-}F/NL\text{-}G\text{-}F}$ mice were used for proteomics analysis. The mouse hippocampus was lysed in 5% SDS and 50 mM triethylammonium bicarbonate (TEAB) supplemented with SIGMAFAST™ protease inhibitor tablets (S8820, Sigma). The protein concentration was determined by BCA (ThermoFisher) using a 96-well plate and analyzed on the VERSA max tunable microplate reader. To create an unbiased pool for normalization across multiple tandem mass tag (TMT) kits, an equal volume of lysates from one-year-old mouse hippocampal samples were combined (Romero et al., 2010). A total of 100 µg of proteins were first reduced with 20 mM dithiothreitol at 95°C for 10 min and then alkylated with 40 mM of iodoacetamide at room temperature in the dark for 30 min. The proteins were subsequently acidified with phosphoric acid and loaded onto the S-trap Micro Spin Column (Protifi, Huntington, New York). Following multiple washes with the S-trap binding buffer (90% methanol and 100 mM of TEAB), trypsin in 50 mM TEAB was introduced into the column and incubated at 37°C overnight. The digested peptides were eluted using a sequence of solutions: 50 mM TEAB, 0.1% formic acid (FA), and 50% acetonitrile (ACN) with 0.1% FA. The peptides were dried down for subsequent TMT isobaric tag labeling.

TMT labeling and liquid chromatography-MS analysis. The peptides were reconstituted into 100 µL of 100 mM TEAB, and each TMT label reagent was resuspended into 41 µL of ACN. The labeling of peptides from each sample was carried out in accordance with the manufacturer's instructions, as detailed in Extended Data Table 3-2. Following labeling, the samples were combined into a single microcentrifuge tube, dried *in vacuo*, and fractionated into 60 fractions using high pH reversed-phase liquid chromatography (LC). To reduce the complexity, these fractions were concatenated into

20 fractions by combining 3 fractions for every 20, and once again dried *in vacuo* (Huang et al., 2020). Each fraction was resuspended into 0.1% v/v FA and injected into a Thermo NanoViper trap column (75 µm × 20 mm, 3 µm C18, 100 Å) (Thermo Fisher Scientific) installed on an Agilent 1260 Infinity nanoLC system (Agilent Technologies) and processed as described previously (Golding et al., 2023). All raw mass spectrometry data can be accessed on the MassIVE data repository (http://massive.ucsd.edu) with project ID MSV000092969.

Protein identification. Raw files from the LC-MS analysis were imported into Proteome Discoverer 2.3 (Thermo Fisher Scientific). These files were processed using the Sequest HT search engine and matched against the SwissProt *Mus musculus* database, which was downloaded in December 2019. In the search parameters, trypsin was specified as the protease, allowing for up to two missed cleavages, and sequences with lengths between 6 and 144 amino acids were considered. The mass error tolerances for precursor and fragment masses were set at 10 ppm and 0.02 Da, respectively. Masses with charges of 1 and larger than 6 were excluded from MS/MS analysis. Dynamic modifications taken into account during the analysis included oxidation (+15.995 Da; M), TMT (+229.163 Da; S, T), and acetylation (+42.011 Da; N-terminus). Static modifications included TMT6plex (+229.163 Da; any N-terminus) and carbamidomethylation (+57.021 Da, C). The quantification of identified proteins was carried out using the MSstatsTMT package, developed by Huang et al. (2020) within the R programming language. All samples were normalized to the unbiased pool sample. Detailed protein identifications are provided in Extended Data Tables 3-4 and 3-5.

Protein annotation and abundance analysis. UniProt accession numbers for each peptide were annotated using the Org.Mm.eg.db and musculus_gene_ensembl databases from the biomaRt package using the R programming language. Non-specific peptides were removed. Principal component analysis (PCA) was performed on the scaled abundance values for each protein using the prcompfunction in R. The CellMarker (CM) 2.0 database (Hu et al., 2023) was used to identify oligodendrocyte-specific proteins using the query "mouse" + "brain" + "oligodendrocyte". Heatmaps for CM protein lists were made using the ComplexHeatmap package in R to compare the scaled abundance values across all samples for each protein. The "CM score" in heatmaps was provided by the CM database "count" field in search results for each gene. Slopegraphs were made by calculating the mean scaled abundance values within each group and calculating the difference between APPKI and wild-type within each age group.

Experimental design and statistical analysis. For FA analyses, a three-way mixed Type II ANOVA was performed using genotype and age group as between-subject variables and the brain ROI as a within-subject variable. The main effects of age, genotype, and ROI, as well as all interaction effects were performed accounting for the within-subject error by ROI. Violations of sphericity were corrected for using Greenhouse-Geisser correction. Statistical analyses were performed using the R programming language version 3.6.3 (R Core Team, 2018). Mixed ANOVA analyses were performed using the afex package (Singmann et al., 2021). *Post hoc* pairwise comparisons were performed using the emmeans package (Lenth, 2021). For Western blot and stereology quantification, Student's independent *t*-test was used to compare groups. Fluoromyelin Red fluorescence intensity quantification was performed by pooling 40 × sum intensity *z*-projection image pixel values from each subject within group. The Kolmogorov–Smirnov (KS) test was used for testing the difference in distributions between groups.

For proteomics analyses, a linear mixed model (LMM) was used to test for the fixed effects of age and genotype across oligodendrocyte-related proteins using the lme4 (Bates et al., 2015) and lmerTest (Kuznetsova et al., 2017) packages in R. The abundance of each protein was standardized. The abundance y_{ij} of the *j*th oligodendrocyte-related protein for the *i*th subject was modeled allowing for a random slope and intercept for age and genotype for each protein, that is,

$$\begin{aligned} y_{ij} = {} & (\beta_0 + u_{0j}) + (\beta_{1j} + u_{1j})\text{Age}_{ij} + (\beta_{2j} + u_{2j})\text{Genotype}_{ij} \\ & + (\beta_{3j} + u_{3j})(\text{Age} \times \text{Genotype})_{ij} + \varepsilon_{ij} \end{aligned} \tag{4}$$

for subjects $i = 1, \ldots, N$, and proteins $j = 1, \ldots, P$, where age and genotype are treated as fixed effects. This was modeled in R as zscore ~ Age * Genotype + (1 + (Age * Genotype) | Symbol). *Post hoc* pairwise comparisons were performed with the emmeanspackage (Lenth, 2021) with Tukey's adjustment for multiple comparisons using emmeans(., list(pairwise ~ Age * Genotype), adjust = "tukey")).

Comparisons of protein abundance between groups were performed using Student's independent *t*-test. Benjamini–Hochberg's false discovery rate was used to correct for multiple comparisons for each comparison.

Software. Neuroimaging analysis and fluorescence quantification were performed using FSL (Jenkinson et al., 2012) and Python version 3.8 (Van Rossum and Drake Jr, 1995) from the Anaconda distribution (Anaconda, 2018) and associated scientific computing libraries, including numpy (Harris et al., 2020), scipy (Virtanen et al., 2020), pandas (McKinney, 2010), scikit-learn (Pedregosa et al., 2011), nibabel (Brett et al., 2020), and nipype (Gorgolewski et al., 2011). Visualization was performed using Python with matplotlib (Hunter, 2007) and seaborn (Waskom, 2021), and R with ggplot2 (Wickham, 2016) and

afex (Singmann et al., 2021) packages. Arrangement of figures was done using GNU Image Manipulation Program version 2.8.16 (Kimball et al., 2016) and Inkscape version 0.92 (Inkscape, 2017). Liquid_Chromatograph_Mass_Spectrometer icon provided by https://bioicons.com/ by DBCLS https://togotv.dbcls.jp/en/pics.html is licensed under CC-BY 4.0 Unported https://creativecommons.org/licenses/by/4.0/.

Results

Reduced FA in APPKI mice in late age

We performed *in vivo* DTI of female wild-type and APPKI mice in early (4 months), middle (10 months), and late (>15 months) age groups (Extended Data Table 1-1) in order to study changes in brain structure with age in the context of FAD. After fitting the tensor model to each image, we measured the mean FA in each brain ROI as a proxy of microstructural integrity (Fig. 1). A three-way mixed Type II ANOVA was performed to test for differences in FA using age group (early, middle, and late) and genotype (wild-type, APPKI) as between-subject factors and treating each ROI as a repeated measure (Fig. 1, Extended Data Table 1-2). There was a statistically significant interaction between age and ROI ($F(7.28, 145.55) = 2.76$, $\eta_g^2 = 0.026$, $p = 0.009$; Extended Data Table 1-3), as well as a statistically significant interaction between genotype and ROI ($F(3.64, 145.55) = 3.14$, $\eta_g^2 = 0.015$, $p = 0.02$; Fig. 1*g*, Extended Data Tables 1-2 and 1-4; additional statistics provided in Extended Data Tables 1-5–1-7). Overall, mice in the late age group and APPKI mice had lower FA compared to other groups. In particular, we observed the largest reductions in FA in the AC, hippocampus, hypothalamus, and neocortex, suggesting that there are microstructural changes in these regions between middle and late age.

APPKI mice show greater oligodendrocytes, less myelin intensity, in the AC in middle age

Since FA is traditionally used as a proxy of WM, we investigated whether there were changes in oligodendrocytes—the myelinating cells of the central nervous system—in APPKI mice in middle age, prior to the reduced FA observed in the DTI. In particular, we examined two of the regions observed to have reduced FA in APPKI mice (Fig. 1*g–h*): the AC, which is a prominent interhemispheric WM tract, and the hippocampus, because of its known vulnerability in AD. We performed blinded unbiased stereology to quantify the number of oligodendrocytes, characterized by the expression of the oligodendrocyte transcription factor 2 (OLIG2), and oligodendrocyte progenitor cells (OPCs), which co-express OLIG2 and the PDGFRA (Pringle and Richardson, 1993; Kuhn et al., 2019). We observed a statistically significant greater number of oligodendrocytes (Student's independent *t*-test, $t(6) = -2.454$, $p = 0.0495$) and no statistically significant difference in the percentage of OPCs (Student's independent *t*-test, $t(6) = 1.81$, $p = 0.12$; Fig. 2*a–c*, Extended Data Tables 2-2 and 2-3).

After observing a higher number of oligodendrocytes in the AC in middle age APPKI mice, we asked whether APPKI mice also had a higher amount of myelin in the AC. To test this, we used the lipophilic dye Fluoroymelin Red and quantified the fluorescence intensity of the AC in both groups (Fig. 2*d*). Interestingly, we observed a reduction in Fluoromyelin Red intensity in APPKI mice (KS test, KS statistic = 0.238, $p < 0.001$; Fig. 2*e–h*). Together, these data suggest that, despite more oligodendrocytes, APPKI mice appeared to have less lipid content. This suggests that in middle age there may be an impairment in myelin homeostasis mechanisms in APPKI mice that deteriorates with age, leading to reduced FA observed in the late age DTI.

APPKI mice have greater number of oligodendrocytes and higher oligodendrocyte-related protein expression in the hippocampus in middle age preceding observable DTI changes

Having observed a greater number of oligodendrocytes in the AC, we next investigated if there were alterations in oligodendrocytes in the hippocampus, which we also observed to have reduced FA in later age. We similarly performed unbiased stereology to quantify the number of oligodendrocytes and OPCs in the hippocampus. As in the AC, we observed a statistically significant greater number of total oligodendrocytes (Student's independent *t*-test, $t(6) = -3.75$, $p = 0.009$) and putative mature oligodendrocytes ($OLIG2^+ PDGFRA^-$ cells; Student's independent *t*-test, $t(6) = -4.19$, $p = 0.006$) in the hippocampus in 10-month-old APPKI mice compared to age-matched wild-type mice, and we observed a slight (not statistically significant) reduction in the percentage of OPCs (Student's independent *t*-test, $t(6) = 2.3068$, $p = 0.06$; Fig. 3*a–c*, Extended Data Table 3-3). We further validated this observation at the protein level using Western analysis and observed a higher expression of OLIG2 in the hippocampus (Student's independent *t*-test, $t(6) = -3.15$, $p = 0.035$; Fig. 3*d* and *e*).

After observing both a greater number of oligodendrocytes and OLIG2 at the protein level in middle age APPKI mice (Fig. 3*b–e*), we explored protein expression near this middle age time window by performing LC-MS proteomics analysis of hippocampal lysate from 6- and 12-month-old WT and APPKI mice (Fig. 3*f*, Extended Data Tables 3-4 and 3-5). First, we computed PCA across all proteins detected for each of the four groups (Fig. 3*f*). The first principal component (PC1) accounted for over 30% of the variance in the data (Extended Data Table 3-6), and largely segregated the four groups according to age (Fig. 3*f*). The second principal component (PC2) accounted for 9.8% of the data (Extended Data Table 3-6) and segregated the four groups by genotype (Fig. 3*f*). This suggests that the largest differences in protein expression were contributed by age and genotype.

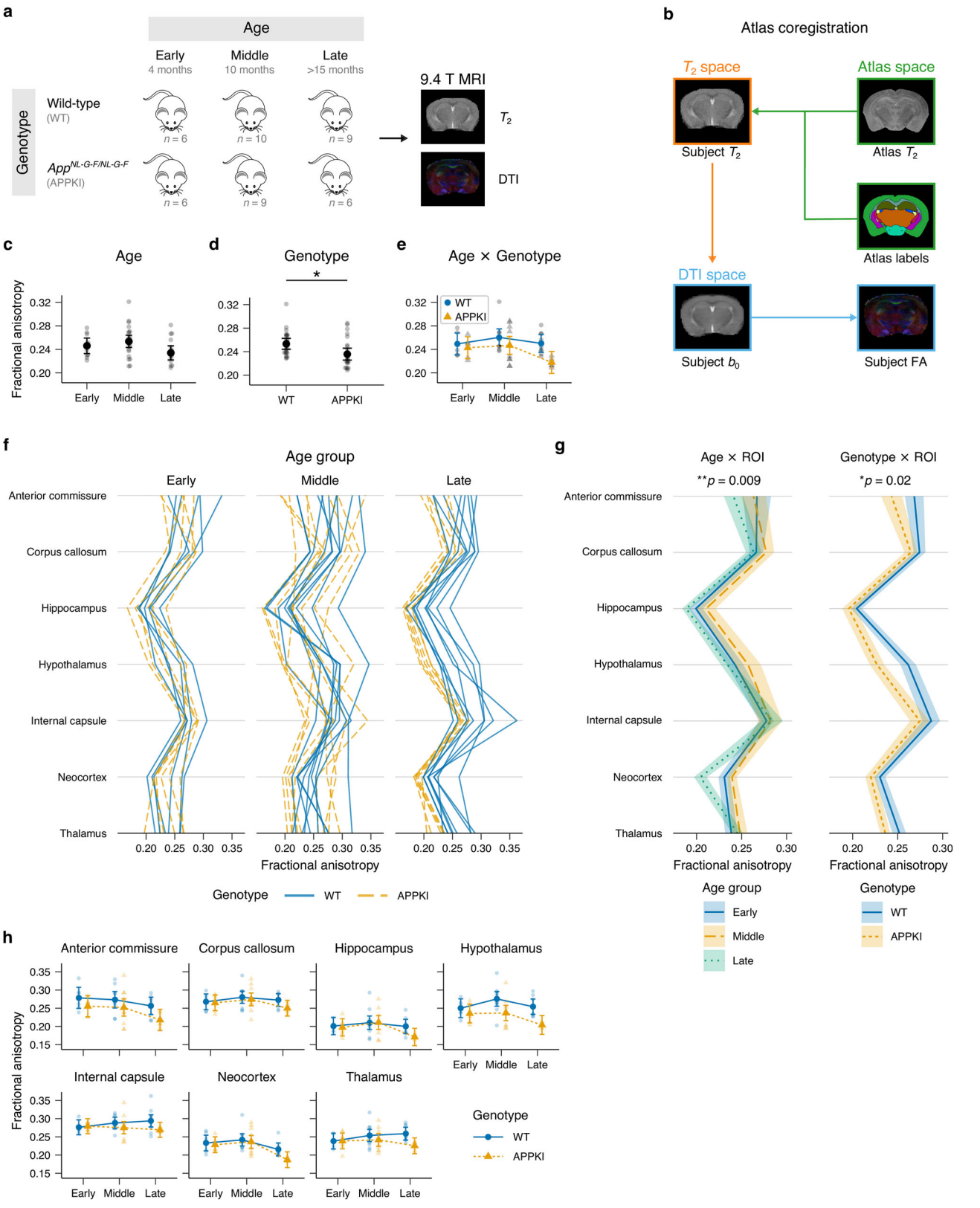

Figure 1. MRI experiment design and *in vivo* FA measurements by age, genotype, and region of interest (ROI). ***a***, *In vivo* MRI scanning paradigm. Wild-type and APPKI female mice were scanned using a 9.4 T MRI system for T_2-weighted and 12-direction DTI sequences. Mice were scanned in early (4 months), middle (10 months), and late (>15 months) age groups. Descriptive statistics for mice is shown in Extended Data Table 1-1. ***b***, Atlas coregistration scheme. High resolution T_2-weighted images from the atlas were registered to each subject's T_2-weighted image. Coregistration was performed to align each subject's T_2-weighted image to their corresponding b_0 image from the DWI sequence. The atlas labels were then registered to each subject's subject space by

We sought to test the hypothesis that oligodendrocyte-related proteins are upregulated in APPKI mice. To do this, we used the CM 2.0 database (Hu et al., 2023) to query proteins associated with oligodendrocytes in the mouse brain. After cross-referencing this list with proteins detected in our sample, we compared the abundance values of proteins with the highest CM scores (i.e., proteins most associated with mouse oligodendrocytes, Fig. 3*h*). We used a LMM to test if there was a greater abundance of oligodendrocyte-related proteins in APPKI mice. There was a statistically significant main effect of age ($t(22.56) = 2.408$, $p = 0.0037$) and a statistically significant interaction between age and genotype ($t(91.53) = 2.31$, $p = 0.0231$; Extended Data Tables 3-7 and 3-8; Fig. 3*i*). *Post hoc* pairwise comparisons showed a statistically significant difference in oligodendrocyte-related protein abundance between 6-month-old WT and 6-month-old APPKI mice ($t(20) = -4.506$, $p = 0.0011$), 12-month-old WT and 12-month-old APPKI mice ($t(20) = -3.606$, $p = 0.0088$), and between 6-month-old APPKI and 12-month-old APPKI mice ($t(20) = -4.307$, $p = 0.0018$; Extended Data Table 3-9). At the level of individual proteins, using a threshold of $q < 0.2$, there was a statistically significant difference in protein abundance in Ermin (ERMN; 6-month-old: APPKI/WT; 12-month-old: APPKI/WT), 2′, 3′-cyclic-nucleotide 3′-phosphodiesterase (CNP), gelsolin (GSN), myelin-associated oligodendrocyte basic protein (MOBP), prostaglandin D_2 synthase (PTGDS; 12-month-old: APPKI/WT), aspartoacylase (ASPA), MBP (APPKI: 12-month-old/6-month-old; statistical details provided in Extended Data Table 3-10). Together, this suggests that the number of oligodendrocytes and multiple oligodendrocyte-related proteins are higher in the hippocampus in middle age APPKI mice prior to structural deficits observed at the macroscale by DTI.

Discussion

In this study, we used the APPKI mouse model (Saito et al., 2014) that harbors three FAD mutations to study structural alterations of the brain across age. We observed reduced FA overall in APPKI and late age mice, especially in the AC, hippocampus, hypothalamus, and neocortex, suggesting that there were microstructural impairments in those regions. Furthermore, Fluoromyelin quantification in the AC suggested that there was reduced myelin content in the APPKI compared to wild-type. To investigate this further at the cellular level, we observed that, by middle age, APPKI mice have a greater oligodendrocyte population in both the hippocampus and the AC. There was also a slight, but not statistically significant ($p = 0.06$), reduction in the percentage of OPCs in the hippocampus. At the molecular level, proteomics analysis of hippocampi from WT and APPKI mice showed a higher expression of oligodendrocyte-related proteins in 12-month-old mice compared to 6-month-old mice, and a significant interaction between age and genotype. Together, this implies that APPKI mice show WM-related alterations by middle age, prior to observed changes by DTI, and that the higher production of oligodendrocytes and oligodendrocyte-related proteins suggests an impaired homeostasis or regulation of oligodendrocytes and myelin.

Previous studies have examined different rodent models of AD using MRI and DTI. Groups that have studied rodents at different age points have generally observed diffusion measurements consistent with measures of microstructural impairment in human AD patients, such as reduced FA, increased radial diffusivity or mean diffusivity, atrophy in GM, and enlargement of the lateral ventricles (Nir et al., 2013; Weston et al., 2015). In GM, changes in volume or DTI measures in the mouse cortex and hippocampus have been reported (Sun et al., 2005; Lau et al., 2008; Qin et al., 2013; Badea et al., 2016; Anckaerts et al., 2019). In WM, changes have been observed in the AC (Sun et al., 2005; Lau et al., 2008; Sahara et al., 2014), internal capsule (Lau et al., 2008; Qin et al., 2013; Badea et al., 2016), external capsule (Anckaerts et al., 2019; Nie et al., 2019), and corpus callosum (Sun et al., 2005; Lau et al., 2008; Anckaerts et al., 2019). The changes observed in DTI begin to appear around middle age, between approximately 8 and 12 months, which is similar to our results where changes in FA were observed after 10 months. While FA is widely used, other measures of tissue integrity including myelin water fraction (MacKay and Laule, 2016), magnetization transfer ratio (Moccia et al., 2020), and neurite orientation dispersion and density imaging (Zhang et al., 2012) may also be informative. Additionally, while our results were obtained *in vivo*, *ex vivo* MRI studies have the potential to offer much higher resolution that can only be achieved with longer acquisition times. Future work combining *ex vivo* imaging and structural connectomics may offer more insight into the network connectivity of the brain in addition to traditional MRI tissue and diffusion measures.

Aging is known to affect both myelin and oligodendrocytes in many brain regions. Across childhood development, Baum et al. (2022) observed that an MRI proxy of myelination was found to increase in a region-specific manner based on their sensorimotor—association axis ranking, such that sensorimotor regions myelinate earlier and association regions myelinate later in adolescence. In the adult, myelination continues and remains relatively stable until approximately 40–50

←

concatenating the previous two transformation matrices. The mean FA was used as the subject measure for each ROI. ***c***–***e***, Main effects of age (***c***) and genotype (***d***) and age × genotype interaction (***e***) for three-way mixed ANOVA model. Gray points represent mean FA for subject. Black points (***c*** and ***d***) and colored points (***e***) represent estimated marginal means for each group. Error bars represent 95% CI. ***f***, Mean FA measurements for each subject for each region. Lines connect observations from each subject. ***h***, Age × ROI and genotype × ROI interactions for the three-way mixed ANOVA model. Lines connect mean FA measurements for each group. Shaded area represents Cousineau–Morey-corrected 95% CI. ***h***, Mean FA measurements for each genotype across age by ROI. Colored points represent estimated marginal means for each group. Gray points represent individual subject means. Error bars represent 95% CI. Additional statistics are provided in Extended Data Table 1-(2-7).

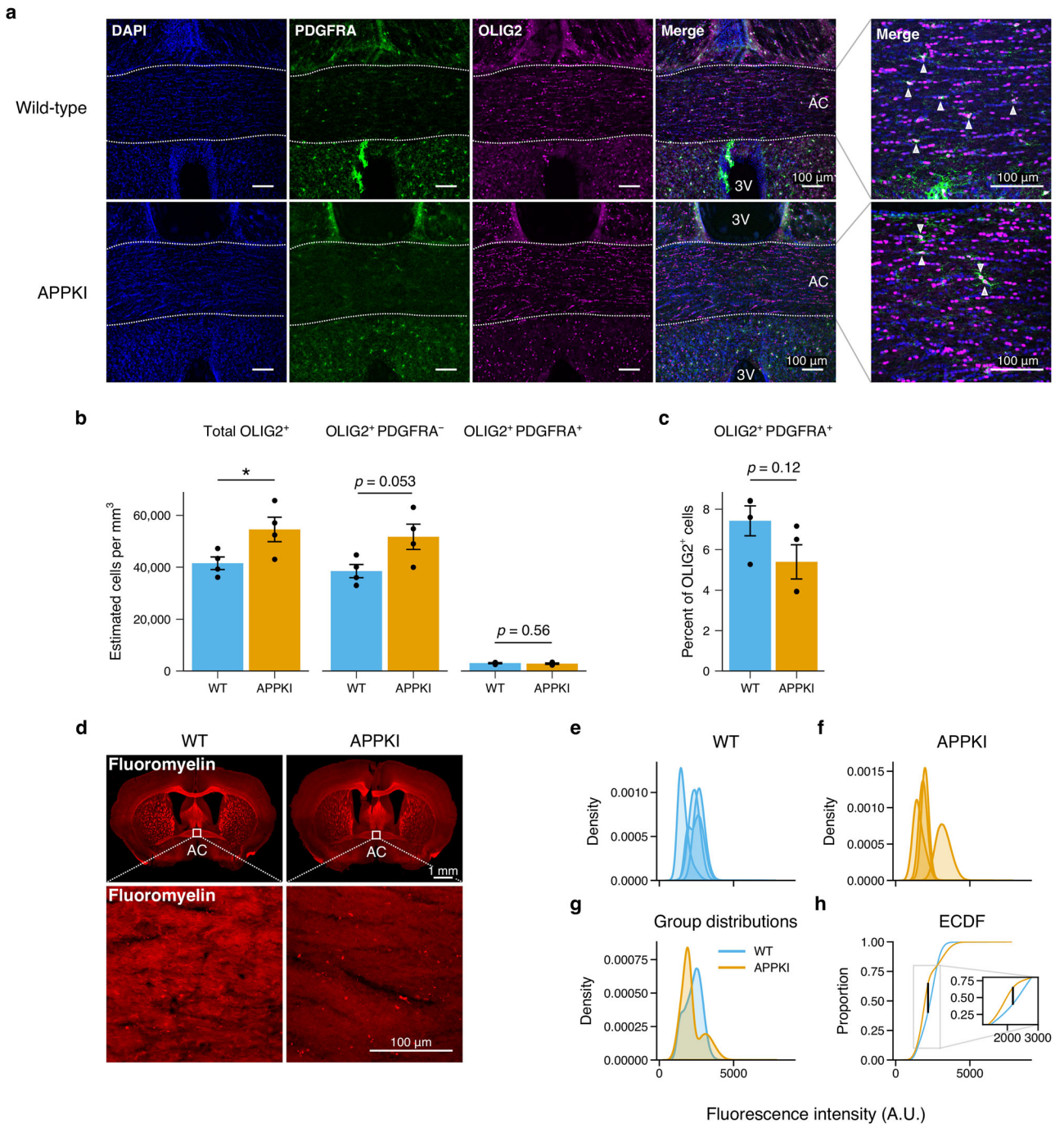

Figure 2. Oligodendrocyte and myelin quantification in the AC in middle age mice. ***a***, Representative confocal images of the midline AC for wild-type and APPKI mice. The AC is outlined in white. High magnification images are shown on the right. White triangles indicate representative OLIG2$^+$ PDGFRA$^+$ cells. AC: anterior commissure; 3V: third ventricle. Scale bars indicate 100 µm. ***b***, Stereological quantification of oligodendrocytes and OPCs. ***c***, Quantification of the percentage of OPCs of the total OLIG2$^+$ population. ***b*** and ***c***, Points represent individual mice ($n = 4$ mice per group); bars represent mean; error bars represent SEM; blue: WT; orange: APPKI. Student's independent *t*-test. *$p < 0.05$. Stereological quantification parameters are described in Extended Data Table 2-1. Individual measurements are described in Extended Data Tables 2-2 and 2-3. ***d***, Representative images of wild-type and APPKI mice stained with Fluoromyelin Red. White squares indicate the location of high magnification images used for quantification. AC: anterior commissure. Scale bars in top row indicate 1 mm. Scale bars in bottom row indicate 100 µm. ***e*** and ***h***, Quantification of Fluoromyelin Red. Kernel density estimation (KDE) of pixel intensity for each subject for wild-type (***e***) and APPKI (***f***) mice. ***g***, Pooled KDE for wild-type and APPKI mice. ***h***, Empirical cumulative distribution function (ECDF) for the pooled pixel values for each group. Black vertical line indicates KS test statistic. Inset depicts a zoomed view of the ECDF at the area of largest difference. A.U.: arbitrary units.

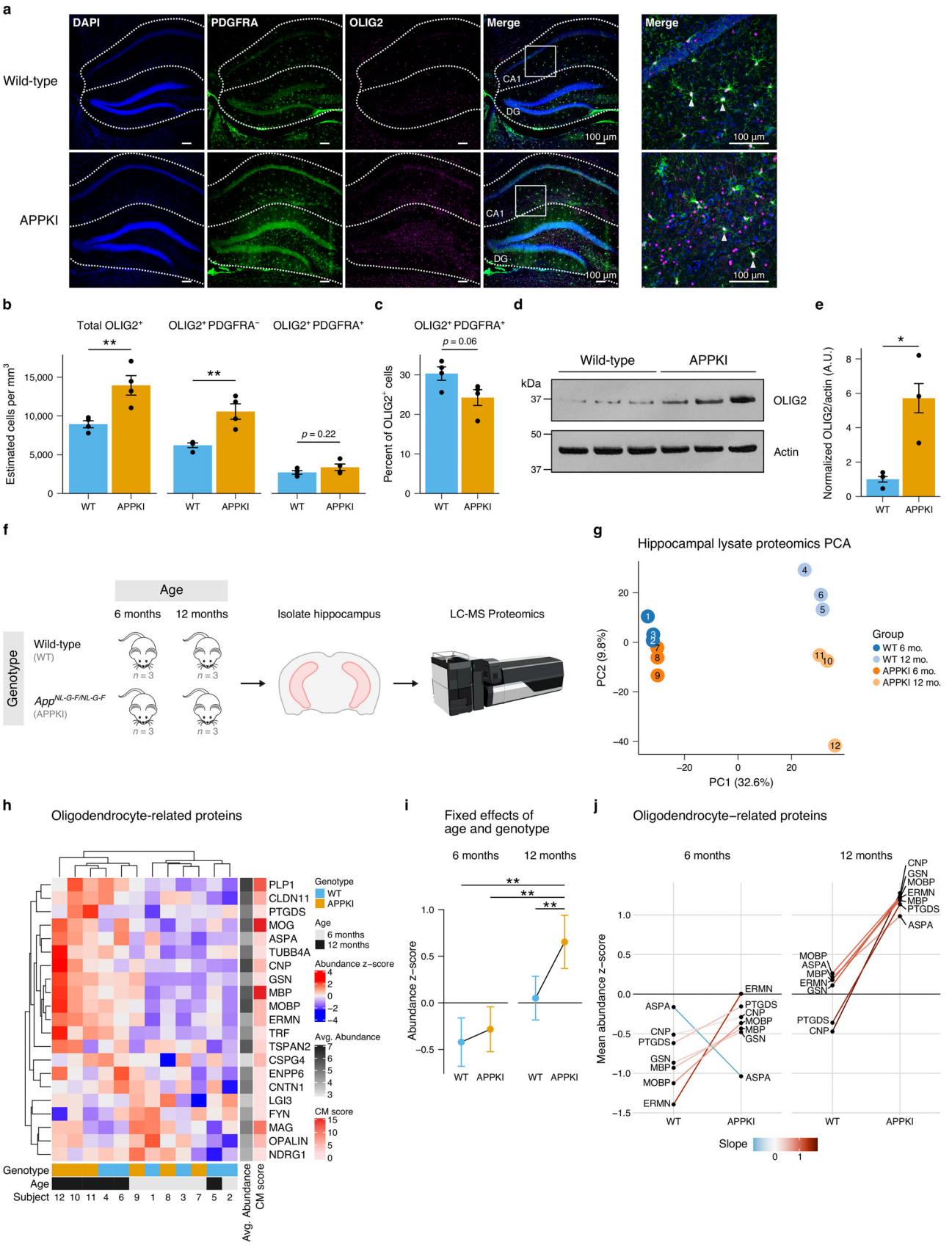

Figure 3. Continued.

years of age, after which there is a notable decline, the rate of which is also region-specific (Bartzokis, 2004, 2011; Langnes et al., 2020). In AD, the pattern of degeneration is notably inverse of the developmental myelination process (Braak et al., 2006), suggesting that association areas that myelinate later in life are the earliest areas of vulnerability in AD (Braak et al., 2006; Bartzokis, 2011).

The microscopic changes in WM likely occur many years before gross changes detected by MRI and the onset of cognitive impairment (Bartzokis, 2004; Jack et al., 2013). Sandell and Peters (2003) observed that the area of the AC in rhesus monkeys, for example, peaks in middle age, but by old age it decreases to below that of young monkeys. At the cellular level, aging leads to an increase in both the density and number of oligodendrocytes in multiple areas of the brain (O'Kusky and Colonnier, 1982; Peters and Sethares, 2004; Peters et al., 2008). Despite the increase in the number of oligodendrocytes, electron microscopy of the AC showed a decrease in the number of myelinated fibers, increase in the number of degenerated axons, and increase in the number of myelin structural alterations with increasing age. Similarly, we did not observe any gross changes in FA until after middle age. This is consistent with both histological and electron microscopy studies in rhesus monkeys as well as the human neuroimaging studies mentioned earlier. In addition to structural changes, there is evidence to suggest that the number of myelinated axon fibers positively correlates with cognitive performance (Sandell and Peters, 2003). Together, these data suggest that alterations in myelin quality, structure, and oligodendrocyte dynamics likely begin in middle age. In the context of AD, the number of oligodendrocytes in APP/PS1 mice were found to be comparable at 3 months of age in GM but significantly increased in GM by 6 months of age (Behrendt et al., 2013). A study by Chen et al. (2021) observed a comparable number of $NG2^+$ $OLIG2^+$ OPCs at 8 months of age in APP/PS1 mice. They also observed more newly formed myelin and degenerated older myelin in APP/PS1 mice compared to controls. Our results with the APPKI are largely consistent with these results; namely, we observed a greater number of oligodendrocytes in middle age APPKI mice and reduced lipid content, which could be indicative of reactive oligodendrocytosis in response to injury (Levine et al., 2001). One interpretation of this could be an increased attempt at myelin repair (Bartzokis, 2011; El Waly et al., 2014), which may be impaired based on the observed reduction of Fluoroymelin fluorescence intensity, in combination with increasing amyloid plaque deposition (Behrendt et al., 2013; Chen et al., 2020), especially given the increased vulnerability of late-myelinating regions (Sachdev et al., 2013; Baum et al., 2022).

Furthermore, the expression of multiple oligodendrocyte-related proteins appeared to be altered in middle age APPKI mice, in particular, ERMN, CNP, GSN, MOBP, PTGDS, ASPA, and MBP. ERMN is a cytoskeletal protein expressed exclusively in CNS myelin, and is thought to aid the arrangement, compaction, and maintenance of myelin in oligodendrocytes (Brockschnieder et al., 2006), and was found to be greater in APPKI relative to WT for both the 6- and 12-month-old groups. CNP is an intracellular protein expressed in oligodendrocytes. It is known to regulate oligodendrocyte differentiation and plays a role in the extension of oligodendrocyte processes for myelin development (Gravel et al., 1996). In the CNS, GSN is expressed predominantly by oligodendrocytes, and is involved in severing and restructuring actin filaments (Tanaka and Sobue, 1994; Vouyiouklis and Brophy, 2002). It is thought to have a role in the formation of myelin (Vouyiouklis and Brophy, 2002). Notably, extracellular GSN has also been shown to interact with amyloid β (Chauhan et al., 1999). MOBP is involved in myelin compaction, stability, regulation of processes, and oligodendrocyte morphology (Gould et al., 2002; Montague et al., 2006; Schäfer et al., 2016). PTGDS is responsible for the production of prostaglandin D_2 in the brain, and has also been shown to be expressed in OPCs (Sakry et al., 2015). ASPA is an enzyme that catalyzes N-acetylaspartic acid into aspartate and acetate, which is critical for the biosynthesis of myelin lipids, and thus is important for WM integrity (Chakraborty et al., 2001; Bitto et al., 2007; Wijayasinghe et al., 2014). Taken together, the alterations in these oligodendrocyte-related proteins suggest that multiple characteristics including oligodendrocyte morphology, processes, and myelin maintenance are affected in later age and APPKI. Future studies using both male and female mice will

←

Figure 3. Oligodendrocyte quantification and proteomics in the hippocampus in middle age mice. ***a***, Representative confocal images of the hippocampus for 10-month-old wild-type and APPKI mice. The DG and CA1 of the hippocampus are outlined. The white squares indicate the location for the high magnification images on the right. White triangles indicate representative $OLIG2^+$ $PDGFRA^+$ cells. Scale bars indicate 100 µm. ***b***, Stereological quantification of oligodendrocytes and OPCs. ***c***, Quantification of the percentage of OPCs of the total $OLIG2^+$ population. Stereological quantification parameters are described in Extended Data Table 3-1. Individual measurements are described in Extended Data Table 3-3. ***d***, Representative Western blot of hippocampal lysate probed for OLIG2 and actin. ***e***, Quantification of membrane in (***d***). A.U.: arbitrary units. ***b***, ***c***, and ***e***, Points represent individual mice ($n = 4$ mice per group). Bars represent mean. Error bars represent SEM. Student's independent *t*-test. $^{**}p < 0.01$; $^{*}p < 0.05$. ***f***, Experiment design for proteomics. Hippocampi were isolated from 6- and 12-month-old WT and APPKI mice and processed for LC-MS proteomics. Details regarding samples and abundnace measurements are described in Extended Data Tables 3-2, 3-4, and 3-5. ***g***, PCA of hippocampal lysate proteomics data obtained from 6- and 12-month-old WT and APPKI mice. Points represent individual subjects; numbers indicate subject ID. Individual PC percentages are shown in Extended Data Table 3-6. ***h***, Heatmap of oligodendrocyte-related proteins detected using the CM 2.0 database query for "mouse" + "brain" + "oligodendrocyte". Color indicates the (row) standardized abundance for each protein for each subject. Gray row annotations indicate the average protein abundance across all subjects. Red row annotations indicate the CM score obtained from the CM database. Higher values indicate proteins most associated with the CM database query. ***i***, Fixed effects of age and genotype for LMM analysis of oligodendrocyte-related proteins. Points represent model fit. Error bars represent 95% CI. Significance code: $^{**}p < 0.01$. ***j***, Slopegraph of oligodendrocyte-related proteins detected in proteomics dataset for 6-month-old and 12-month-old WT and APPKI mice with at least one $q < 0.2$ pairwise comparison. Points indicate mean abundance *z*-score for given protein for each group. Lines connect the same protein between WT and APPKI. Color of line indicates slope difference between WT and APPKI within each age group. Additional statistics are provided in Extended Data Table 3-(7-10).

be informative to know if there are sex-specific differences in the expression of these proteins, since there are known sex differences in oligodendrocyte dynamics (Cerghet et al., 2006) and AD (Li and Singh, 2014; Mazure and Swendsen, 2016). Additionally, future studies could also address the functional implications of these changes in oligodendrocytes and the possible mechanism by which this occurs, as well as in other areas of the brain.

In summary, we used a combination of DTI, molecular biology, and proteomics to investigate temporal changes in WM using the $App^{NL\text{-}G\text{-}F/NL\text{-}G\text{-}F}$ mouse model of AD. We observed alterations in oligodendrocyte homeostasis and expression profile in the hippocampus in middle age, preceding reduced integrity measured by DTI in later age. Together, these results provide potential therapeutic biomarkers and a better understanding of the early progression of AD.

References

Anaconda (2018) *Anaconda software distribution*. Anaconda.

Anckaerts C, Blockx I, Summer P, Michael J, Hamaide J, Kreutzer C, Boutin H, Couillard-Després S, Verhoye M, Van der Linden A (2019) Early functional connectivity deficits and progressive microstructural alterations in the TgF344-AD rat model of Alzheimer's disease: a longitudinal MRI study. Neurobiol Dis 124:93–107.

Badea A, et al. (2016) The fornix provides multiple biomarkers to characterize circuit disruption in a mouse model of Alzheimer's disease. NeuroImage 142:498–511.

Bartzokis G (2004) Age-related myelin breakdown: a developmental model of cognitive decline and Alzheimer's disease. Neurobiol Aging 25:5–18.

Bartzokis G (2011) Alzheimer's disease as homeostatic responses to age-related myelin breakdown. Neurobiol Aging 32:1341–1371.

Basser P, Mattiello J, LeBihan D (1994) MR diffusion tensor spectroscopy and imaging. Biophys J 66:259–267.

Bates D, Mächler M, Bolker B, Walker S (2015) Fitting linear mixed-effects models using lme4. J Stat Softw 67:1–48.

Baum GL, et al. (2022) Graded variation in T1w/T2w ratio during adolescence: measurement, caveats, and implications for development of cortical myelin. J Neurosci 42:5681–5694.

Behrendt G, Baer K, Buffo A, Curtis MA, Faull RL, Rees MI, Götz M, Dimou L (2013) Dynamic changes in myelin aberrations and oligodendrocyte generation in chronic amyloidosis in mice and men. Glia 61:273–286.

Bitto E, Bingman CA, Wesenberg GE, McCoy JG, Phillips GN (2007) Structure of aspartoacylase, the brain enzyme impaired in Canavan disease. Proc Natl Acad Sci U S A 104:456–461.

Blakemore WF (1972) Observations on oligodendrocyte degeneration, the resolution of status spongiosus and remyelination in cuprizone intoxication in mice. J Neurocytol 1:413–426.

Bozzali M (2002) White matter damage in Alzheimer's disease assessed in vivo using diffusion tensor magnetic resonance imaging. J Neurol Neurosurg Psychiatry 72:742–746.

Braak H, Rüb U, Schultz C, Tredici KD (2006) Vulnerability of cortical neurons to Alzheimer's and Parkinson's diseases. J Alzheimers Dis 9:35–44.

Brett M, et al. (2020) Nipy/nibabel: 3.1.1. Zenodo.

Brockschnieder D, Sabanay H, Riethmacher D, Peles E (2006) Ermin, a myelinating oligodendrocyte-specific protein that regulates cell morphology. J Neurosci 26:757–762.

Brun A, Englund E (1986) A white matter disorder in dementia of the Alzheimer type: a pathoanatomical study. Ann Neurol 19:253–262.

Cerghet M, Skoff RP, Bessert D, Zhang Z, Mullins C, Ghandour MS (2006) Proliferation and death of oligodendrocytes and myelin proteins are differentially regulated in male and female rodents. J Neurosci 26:1439–1447.

Chakraborty G, Mekala P, Yahya D, Wu G, Ledeen RW (2001) Intraneuronal N-acetylaspartate supplies acetyl groups for myelin lipid synthesis: evidence for myelin-associated aspartoacylase: N-acetylaspartate for synthesis of myelin lipids. J Neurochem 78:736–745.

Chauhan VPS, Ray I, Chauhan A, Wisniewski HM (1999) Binding of Gelsolin, a secretory protein, to amyloid β-protein. Biochem Biophys Res Commun 258:241–246.

Chen W-T, et al. (2020) Spatial transcriptomics and in situ sequencing to study Alzheimer's disease. Cell 182:976–991.e19.

Chen J-F (2021) Enhancing myelin renewal reverses cognitive dysfunction in a murine model of Alzheimer's disease. Neuron 109:2292–2307.

El Waly B, Macchi M, Cayre M, Durbec P (2014) Oligodendrogenesis in the normal and pathological central nervous system. Front Neurosci 8:1–22.

Fischer FU, Wolf D, Scheurich A, Fellgiebel A (2015) Altered whole-brain white matter networks in preclinical Alzheimer's disease. NeuroImage Clin 8:660–666.

Fox NC, Warrington EK, Freeborough PA, Hartikainen P, Kennedy AM, Stevens JM, Rossor MN (1996) Presymptomatic hippocampal atrophy in Alzheimer's disease: a longitudinal MRI study. Brain 119:2001–2007.

Golding AE, Li W, Blank PS, Cologna SM, Zimmerberg J (2023) Relative quantification of progressive changes in healthy and dysferlin-deficient mouse skeletal muscle proteomes. Muscle Nerve 68:805–816.

Gorgolewski K, Burns CD, Madison C, Clark D, Halchenko YO, Waskom ML, Ghosh SS (2011) Nipype: a flexible, lightweight and extensible neuroimaging data processing framework in python. Front Neuroinformatics 5:1–15.

Gould RM, Freund CM, Palmer F, Feinstein DL (2002) Messenger RNAs located in myelin sheath assembly sites. J Neurochem 75:1834–1844.

Gravel M, Peterson J, Yong VW, Kottis V, Trapp B, Braun PE (1996) Overexpression of 2′,3′-cyclic nucleotide 3′-phosphodiesterase in transgenic mice alters oligodendrocyte development and produces aberrant myelination. Mol Cell Neurosci 7:453–466.

Gundersen HJG, Jensen EB (1987) The efficiency of systematic sampling in stereology and its prediction*. J Microsc 147:229–263.

Gundersen HJG, Jensen EBV, Kieu K, Nielsen J (1999) The efficiency of systematic sampling in stereology—reconsidered. J Microsc 193:199–211.

Harris CR, et al. (2020) Array programming with NumPy. Nature 585:357–362.

Hill RA, Li AM, Grutzendler J (2018) Lifelong cortical myelin plasticity and age-related degeneration in the live mammalian brain. Nat Neurosci 21:683–695.

Hu C, et al. (2023) CellMarker 2.0: an updated database of manually curated cell markers in human/mouse and web tools based on scRNA-seq data. Nucleic Acids Res 51:D870–D876.

Huang T, Choi M, Tzouros M, Golling S, Pandya NJ, Banfai B, Dunkley T, Vitek O (2020) MSstatsTMT: statistical detection of differentially abundant proteins in experiments with isobaric labeling and multiple mixtures. Mol Cell Proteom 19:1706–1723.

Hughes EG, Kang SH, Fukaya M, Bergles DE (2013) Oligodendrocyte progenitors balance growth with self-repulsion to achieve homeostasis in the adult brain. Nat Neurosci 16:668–676.

Hunter JD (2007) Matplotlib: a 2D graphics environment. Comput Sci Eng 9:90–95.
Inkscape (2017) Inkscape version 0.92.5. https://inkscape.org/.
Jack CR, et al. (2013) Tracking pathophysiological processes in Alzheimer's disease: an updated hypothetical model of dynamic biomarkers. Lancet Neurol 12:207–216.
Jenkinson M, Beckmann CF, Behrens TE, Woolrich MW, Smith SM (2012) FSL. NeuroImage 62:782–790.
Johnson GA, Badea A, Brandenburg J, Cofer G, Fubara B, Liu S, Nissanov J (2010) Waxholm space: an image-based reference for coordinating mouse brain research. NeuroImage 53:365–372.
Kaplan MS, Hinds JW (1980) Gliogenesis of astrocytes and oligodendrocytes in the neocortical grey and white matter of the adult rat: electron microscopic analysis of light radioautographs. J Comp Neurol 193:711–727.
Keuker JI, Vollmann-Honsdorf GK, Fuchs E (2001) How to use the optical fractionator: an example based on the estimation of neurons in the hippocampal CA1 and CA3 regions of tree shrews. Brain Res Protoc 7:211–221.
Kimball S, Matthis, P, and the GIMP Development Team (2016) GNU Image Manipulation Program version 2.8.16. https://www.gimp.org/.
Kuhn S, Gritti L, Crooks D, Dombrowski Y (2019) Oligodendrocytes in development, myelin generation and beyond. Cells 8:1424.
Kuznetsova A, Brockhoff PB, Christensen RHB (2017) lmerTest package: tests in linear mixed effects models. J Stat Softw 82:1–26.
Langnes E, Sneve MH, Sederevicius D, Amlien IK, Walhovd KB, Fjell AM (2020) Anterior and posterior hippocampus macro-and microstructure across the lifespan in relation to memory—a longitudinal study. Hippocampus 30:678–692.
Lau JC, Lerch JP, Sled JG, Henkelman RM, Evans AC, Bedell BJ (2008) Longitudinal neuroanatomical changes determined by deformation-based morphometry in a mouse model of Alzheimer's disease. NeuroImage 42:19–27.
Lenth RV (2021) Emmeans: estimated marginal means, AKA least-squares means. R package version 1.6.0. https://CRAN.R-project.org/package=emmeans.
Levine JM, Reynolds R, Fawcett JW (2001) The oligodendrocyte precursor cell in health and disease. Trends Neurosci 24:39–47.
Li X (2016) The first step for neuroimaging data analysis: DICOM to NIfTI conversion. J Neurosci Methods 264:47–56.
Li R, Singh M (2014) Sex differences in cognitive impairment and Alzheimer's disease. Front Neuroendocrinol 35:385–403.
Lo Buono V, Palmeri R, Corallo F, Allone C, Pria D, Bramanti P, Marino S (2020) Diffusion tensor imaging of white matter degeneration in early stage of Alzheimer's disease: a review. Int J Neurosci 130:243–250.
MacKay AL, Laule C (2016) Magnetic resonance of myelin water: an in vivo marker for myelin. Brain Plast 2:71–91.
Mazure CM, Swendsen J (2016) Sex differences in Alzheimer's disease and other dementias. Lancet Neurol 15:451–452.
McKenzie IA, Ohayon D, Li H, De Faria JP, Emery B, Tohyama K, Richardson WD (2014) Motor skill learning requires active central myelination. Science 346:318–322.
McKinney W (2010) Data structures for statistical computing in python. Proceedings of the 9th python in science conference. p 6. Scipy 2010.
McNamara NB, Miron VE (2021) Replenishing our mind orchards: enhancing myelin renewal to rescue cognition in Alzheimer's disease. Neuron 109:2204–2206.
Menn B, Garcia-Verdugo JM, Yaschine C, Gonzalez-Perez O, Rowitch D, Alvarez-Buylla A (2006) Origin of oligodendrocytes in the subventricular zone of the adult brain. J Neurosci 26:7907–7918.
Moccia M, et al. (2020) Pathologic correlates of the magnetization transfer ratio in multiple sclerosis. Neurology 95:e2965–e2976.
Montague P, McCallion AS, Davies RW, Griffiths IR (2006) Myelin-associated oligodendrocytic basic protein: a family of abundant CNS myelin proteins in search of a function. Dev Neurosci 28:479–487.
Morrissey ZD, et al. (2023) Hippocampal functional connectivity across age in an app knock-in mouse model of Alzheimer's disease. Front Aging Neurosci 14:1085989.
Nasrabady SE, Rizvi B, Goldman JE, Brickman AM (2018) White matter changes in Alzheimer's disease: a focus on myelin and oligodendrocytes. Acta Neuropathol Commun 6:22.
Nie X, Falangola MF, Ward R, McKinnon ET, Helpern JA, Nietert PJ, Jensen JH (2019) Diffusion MRI detects longitudinal white matter changes in the 3xTg-AD mouse model of Alzheimer's disease. Magn Reson Imaging 57:235–242.
Nir TM, Jahanshad N, Villalon-Reina JE, Toga AW, Jack CR, Weiner MW, Thompson PM (2013) Effectiveness of regional DTI measures in distinguishing Alzheimer's disease, MCI, and normal aging. NeuroImage Clin 3:180–195.
O'Kusky J, Colonnier M (1982) Postnatal changes in the number of astrocytes, oligodendrocytes, and microglia in the visual cortex (area 17) of the macaque monkey: a stereological analysis in normal and monocularly deprived animals. J Comp Neurol 210:307–315.
Pedregosa F, et al. (2011) Scikit-learn: machine learning in python. J Mach Learn Res 12:2825–2830.
Peters A, Sethares C (2004) Oligodendrocytes, their progenitors and other neuroglial cells in the aging primate cerebral cortex. Cereb Cortex 14:995–1007.
Peters A, Verderosa A, Sethares C (2008) The neuroglial population in the primary visual cortex of the aging rhesus monkey: neuroglial cells and aging in cerebral cortex. Glia 56:1151–1161.
Pringle N, Richardson W (1993) A singularity of PDGF alpha-receptor expression in the dorsoventral axis of the neural tube may define the origin of the oligodendrocyte lineage. Development 117:525–533.
Qin Y-Y, Li M-W, Zhang S, Zhang Y, Zhao L-Y, Lei H, Oishi K, Zhu W-Z (2013) In vivo quantitative whole-brain diffusion tensor imaging analysis of APP/PS1 transgenic mice using voxel-based and atlas-based methods. Neuroradiology 55:1027–1038.
R Core Team (2018) *R: a language and environment for statistical computing*. Vienna: R Foundation for Statistical Computing.
Ridha BH, Barnes J, Bartlett JW, Godbolt A, Pepple T, Rossor MN, Fox NC (2006) Tracking atrophy progression in familial Alzheimer's disease: a serial MRI study. Lancet Neurol 5:828–834.
Romero R, et al. (2010) Isobaric labeling and tandem mass spectrometry: a novel approach for profiling and quantifying proteins differentially expressed in amniotic fluid in preterm labor with and without intra-amniotic infection/inflammation. J Matern-Fetal Neonatal Med 23:261–280.
Sachdev PS, Zhuang L, Braidy N, Wen W (2013) Is Alzheimer's a disease of the white matter? Curr Opin Psychiatry 26:244–251.
Sahara N, Perez PD, Lin W-L, Dickson DW, Ren Y, Zeng H, Lewis J, Febo M (2014) Age-related decline in white matter integrity in a mouse model of tauopathy: an in vivo diffusion tensor magnetic resonance imaging study. Neurobiol Aging 35:1364–1374.
Saito T, Matsuba Y, Mihira N, Takano J, Nilsson P, Itohara S, Iwata N, Saido TC (2014) Single App knock-in mouse models of Alzheimer's disease. Nat Neurosci 17:661–663.
Sakry D, Yigit H, Dimou L, Trotter J (2015) Oligodendrocyte precursor cells synthesize neuromodulatory factors. PLoS One 10:e0127222.
Sandell JH, Peters A (2003) Disrupted myelin and axon loss in the anterior commissure of the aged rhesus monkey. J Comp Neurol 466:14–30.
Schäfer I, Müller C, Luhmann HJ, White R (2016) MOBP levels are regulated by Fyn kinase and affect the morphological differentiation of oligodendrocytes. J Cell Sci. 129:930–942.
Schindelin J, et al. (2012) Fiji: an open-source platform for biological-image analysis. Nat Methods 9:676–682.
Singmann H, Bolker B, Westfall J, Aust F, Ben-Shachar MS (2021) Afex: analysis of factorial experiments. R package version 0.28-1. https://CRAN.R-project.org/packages=afex.

Smith SM, et al. (2004) Advances in functional and structural MR image analysis and implementation as FSL. NeuroImage 23:S208–S219.
Steadman PE, Xia F, Ahmed M, Mocle AJ, Penning AR, Geraghty AC, Steenland HW, Monje M, Josselyn SA, Frankland PW (2020) Disruption of oligodendrogenesis impairs memory consolidation in adult mice. Neuron 105:150–164.e6.
Stereo Investigator (2020) Stereo Investigator version 2020.2.3, date October 21, 2020, by MBF Bioscience (MicroBrightField, Inc.).
Sun S-W, Song S-K, Harms MP, Lin S-J, Holtzman DM, Merchant KM, Kotyk JJ (2005) Detection of age-dependent brain injury in a mouse model of brain amyloidosis associated with Alzheimer's disease using magnetic resonance diffusion tensor imaging. Exp Neurol 191:77–85.
Tanaka J, Sobue K (1994) Localization and characterization of gelsolin in nervous tissues: gelsolin is specifically enriched in myelin-forming cells. J Neurosci 14:1038–1052.
Van Rossum G, Drake Jr FL (1995) Python reference manual. Amsterdam: Centrum Voor Wiskunde En Informatica.
Vanzijl P, Sukumar S, Johnson M, Webb P, Hurd R (1994) Optimized shimming for high-resolution NMR using three-dimensional image-based field mapping. J Magn Reson Ser A 111:203–207.
Virtanen P, et al. (2020) SciPy 1.0: fundamental algorithms for scientific computing in Python. Nat Methods 17:261–272.
Vouyiouklis DA, Brophy PJ (2002) A novel gelsolin isoform expressed by oligodendrocytes in the central nervous system. J Neurochem 69:995–1005.
Waskom M (2021) Seaborn: statistical data visualization. J Open Source Softw 6:3021.
Webster SJ, Bachstetter AD, Nelson PT, Schmitt FA, Van Eldik LJ (2014) Using mice to model Alzheimer's dementia: an overview of the clinical disease and the preclinical behavioral changes in 10 mouse models. Front Genet 5:1–23.
Weston PS, Simpson IJ, Ryan NS, Ourselin S, Fox NC (2015) Diffusion imaging changes in grey matter in Alzheimer's disease: a potential marker of early neurodegeneration. Alzheimer's Res Ther 7:47.
Wickham H (2016) Ggplot2: elegant graphics for data analysis. New York: Springer-Verlag.
Wijayasinghe YS, Pavlovsky AG, Viola RE (2014) Aspartoacylase catalytic deficiency as the cause of canavan disease: a structural perspective. Biochemistry 53:4970–4978.
Williamson JM, Lyons DA (2018) Myelin dynamics throughout life: an ever-changing landscape? Front Cell Neurosci 12:424.
Xin W, Chan JR (2020) Myelin plasticity: sculpting circuits in learning and memory. Nat Rev Neurosci 21:682–694.
Zhang H, Schneider T, Wheeler-Kingshott CA, Alexander DC (2012) NODDI: practical in vivo neurite orientation dispersion and density imaging of the human brain. NeuroImage 61:1000–1016.